American Society of Mechanical Engineers

ASME Accepted Manuscript Repository

ASME Paper
Title: Aerodynamic design of separate-jet exhausts for future civil aero engines, part I: parametric

geometry definition and CFD approach

Authors: Ioannis Goulos, Tomasz Stankowski, John Otter, David MacManus, Nicholas Grech, Christopher Sheaf

ASME Journal
Title: Journal of Engineering for Gas Turbines and Power

Volume/Issue: _ __Vol. 138, Iss. 8, Paper GTP-15-1538   Date of Publication (VOR* Online) 15 March 2016_____

ASME Digital Collection   https://asmedigitalcollection.asme.org/gasturbinespower/article/138/8/081201/474642/Aero
URL: dynamic-Design-of-Separate-Jet-Exhausts-for

DOI: https://doi.org/10.1115/1.4032649

*VOR (version of record)

Aerodynamic Design of Separate-Jet Exhausts for Future Civil Aero-Engines, Part 1: Parametric Geometry Definition and CFD Approach

Ioannis Goulos
Propulsion Engineering Centre
Cranfield University
Bedfordshire, MK430AL, UK
Email: i.goulos@cranfield.ac.uk

Tomasz Stankowski
Propulsion Engineering Centre
Cranfield University
Bedfordshire, MK430AL, UK
Email: t.stankowski@cranfield.ac.uk

John Otter
Propulsion Engineering Centre
Cranfield University
Bedfordshire, MK430AL, UK
Email: j.j.otter@cranfield.ac.uk

David MacManus
Propulsion Engineering Centre
Cranfield University
Bedfordshire, MK430AL, UK
Email: D.G.Macmanus@cranfield.ac.uk

Nicholas Grech
Installation Aerodynamics
Rolls-Royce plc
Trent Hall 2.2, SinA-17, Derby, UK
Email: Nicholas.Grech@Rolls-Royce.com

Christopher Sheaf
Installation Aerodynamics
Rolls-Royce plc
Trent Hall 2.2, SinA-17, Derby, UK
Email: Christopher.Sheaf@Rolls-Royce.com

ABSTRACT

This paper presents the development of an integrated approach which targets the aerodynamic design of separate-jet exhaust systems for future gas-turbine aero-engines. The proposed framework comprises a series of fundamental modeling theories which are applicable to engine performance simulation, parametric geometry definition, viscous/compressible flow solution, and Design Space Exploration (DSE). A mathematical method has been developed based on Class-Shape Transformation (CST) functions for the geometric design of axi-symmetric engines with separate-jet exhausts. Design is carried out based on a set of standard nozzle design parameters along with the flow capacities established from zero-dimensional (0D) cycle analysis. The developed approach has been coupled with an automatic mesh generation and a Reynolds Averaged NavierStokes (RANS) flow-field solution method, thus forming a complete aerodynamic design tool for separate-jet exhaust systems.

The employed aerodynamic method has initially been validated against experimental measurements conducted on a small-scale Turbine Powered Simulator (TPS) nacelle. The developed tool has been subsequently coupled with a comprehensive DSE method based on Latin- Hypercube Sampling (LHS). The overall framework has been deployed to investigate the design space of two civil aero-engines with separate jet exhausts, representative of current and future architectures, respectively. The inter-relationship between the exhaust systems' thrust and discharge coefficients has been thoroughly quantified. The dominant design variables that affect the aerodynamic performance of both investigated exhaust systems have been determined. A comparative evaluation has been carried

out between the optimum exhaust design sub-domains established for each engine. The proposed method enables the aerodynamic design of separate-jet exhaust systems for a designated engine cycle, using only a limited set of intuitive design variables. Furthermore, it enables the quantification and correlation of the aerodynamic behavior of separate-jet exhaust systems for designated civil aero-engine architectures. Therefore, it constitutes an enabling technology towards the identification of the fundamental aerodynamic mechanisms that govern the exhaust system performance for a user-specified engine cycle.

Nomenclature

Roman Symbols

$\dot{m}$	Nozzle mass flow, kg/sec
A	Area, m^2
A_{ratio}	Nozzle exit to charging plane area ratio, $= \dfrac{A_{CP}}{A_{exit}}$
$A_r, r = 1,...n$	CST shape function coefficients
$C(x)$	CST Class function
C_D^{Bypass}	Bypass exhaust nozzle discharge coefficient
C_D^{Core}	Core exhaust nozzle discharge coefficient
$C_V^{Overall}$	Exhaust system overall velocity coefficient
C_D^{Zone3}	Zone 3 vent exhaust nozzle discharge coefficient
D_{domain}	Diameter of computational domain, m
D_f	Computational domain diameter scaling factor, m
D_{nac}	Maximum nacelle diameter, m
F_G, F_N	Gross and net propulsive force, N
H, Θ, E	CST analytical spatial functions
h_1	Nozzle charging plane height, m
h_2	Nozzle exit plane height, m
L	Length, m
l_{cr}^{cowl}	Non-dimensional core cowl length, $= \dfrac{L_{cr}^{cowl}}{R_{fan}}$
l_{z3}^{exit}	Non-dimensional location of zone 3 vent exhaust exit, $= \dfrac{L_{z3}^{exit}}{L_{cr}^{cowl}}$
M_∞	Mach number (free-stream)
M_{z3}^{exit}	Zone 3 vent exhaust exit Mach number, $= \dfrac{L_{z3}^{exit}}{L_{cr}^{cowl}}$
N	Range of DOE samples
n	Order of Bernstein polynomial
N_1, N_2	CST class function parameters
P	Pressure, Pa

R	Radius, m
$R(\%)$	Percentage range
R_{CP}^{offset}	Charging plane radial offset relative to the nozzle exit plane, m
R_{curve}	Curvature radius, m
R_{fan}	Fan blade radius, m
$S(x)$	CST Shape function
T	Temperature, K
$x, y(x)$	Normalized CST coordinates
y_{bp}^{in}	Bypass duct normalized inner line radius, $= \dfrac{R_{bp}^{in}}{L_{duct}^{in}}$
y_{bp}^{out}	Bypass duct normalized outer line radius, $= \dfrac{R_{bp}^{out}}{L_{duct}^{in}}$
y_{offset}	Normalized CST offset in the normal direction

Greek Symbols

κ_{CP}^{in}	Inner aeroline curvature radius ratio, $= \dfrac{R_{curve}^{CP,in}}{h_2}$
κ_{CP}^{out}	Outer aeroline curvature radius ratio, $= \dfrac{R_{curve}^{CP,out}}{h_2}$
κ_{len}^{in}	Nozzle length ratio, $= \dfrac{L_{in}^{Nozzle}}{h_2}$
λ	Total to static nozzle pressure ratio
$\sigma(\%)$	Percentage standard deviation
θ_{CP}^{out}	Outer aeroline slope at the charging plane, deg
θ_{cp}^{plug}	Core plug after-body angle, deg
θ_{cr}^{cowl}	Core cowl angle, deg
$\theta_{in/out}^{hade}$	Aeroline hade angle at the nozzle inlet plane, deg
θ_{nozzle}^{out}	Nozzle outer line exit angle, deg

Superscripts

$()', ()''$	First and second derivatives with respect to the normalized CST independent ordinate x
$()^{amb}$	Referring to ambient conditions
$()^{in/out}$	Referring to the inner or outer nozzle aeroline, respectively
$()^{inlet}$	Referring to inlet conditions
$()^{Overall}$	Referring to the overall exhaust system

Subscripts

$()_0$	Referring to total flow conditions
$()_{Actual}$	Referring to actual flow conditions
$()_{bp}$	Referring to the bypass exhaust nozzle
$()_{CP}$	Referring to the nozzle charging plane
$()_{crit}$	Referring to critical flow conditions

$()_{cr}$	Referring to the core exhaust nozzle
$()_{Exit}$	Referring to the nozzle exit plane
$()_{Ideal}$	Referring to ideal flow conditions
$()_{st}$	Referring to static flow conditions
$()_{z3}$	Referring to the zone 3 vent exhaust nozzle

1 Introduction

1.1 Background

Within the context of civil aviation, there is a continuing need to improve the operational performance and environmental impact of integrated aircraft–poweplant systems. This entails, among others, the introduction of more fuel efficient, cost-effective, and environmentally friendly aircraft engines. Epstein [1] pointed out that in order to conceptualize, design, and implement the next generation of civil turbofan engines, substantial advancements need to be achieved with respect to the technologies employed in the design of both motors and propulsors. Considering simple-cycle engine architectures, it is almost certain that future configurations will favor the selection of cycles with increased Turbine Entry Temperature (TET) and Overall Pressure Ratio (OPR) to improve the motor's thermal efficiency [1,2]. The introduction of novel intercooled and intercooled–recuperated thermodynamic cycles has also been investigated by Kyprianidis *et al.* [3–5] with promising results.

With respect to the envisaged propulsor designs of future turbofan engines, it is anticipated that modern configurations will employ higher values of By-Pass Ratio ($BPR = \frac{\dot{m}_{bypass}}{\dot{m}_{core}}$) combined with lower Fan Pressure Ratios (FPR) to lower specific thrust and improve propulsive efficiency [6]. Specifically, it is expected that future large turbofan engines will employ a BPR of the order of 15+ at Design Point (DP) mid-cruise conditions. This is more than 36% higher compared to the BPR of current large turbofan engines which is typically closer to 11. However, a rise in BPR also results in higher gross to net propulsive force ratio $\frac{F_G}{F_N}$. This is due to the larger overall engine mass flow $\dot{m}_{inlet}$ resulting in higher inlet momentum drag which is compensated by augmenting the gross propulsive force F_G. As an indicative example it is noted that the ratio $\frac{F_G}{F_N}$ changes from roughly 3 to 4 for increasing the BPR from 11 to 16, respectively. Concurrently, the net propulsive force F_N and SFC of future turbofan engines will be more sensitive to variations in gross propulsive force F_G compared to current engine architectures.

It is well known that F_G is linearly dependent on the aerodynamic performance of the exhaust system and its ability to produce thrust that is close to its ideal isentropic value [7–9]. Furthermore, the required increase in BPR essentially leads to a higher-amount of mass flow exhausted through the bypass exhaust nozzle relative to the core flow. Hence, with respect to future engine architectures that encompass high values of BPR, the overall performance of the engine will be highly dependent on the aerodynamic design of the bypass duct, nozzle, and post-exit components. It is therefore imperative that the design space governing the exhaust's performance is thoroughly explored and understood to enable the selection and implementation of potential design solutions in an optimum and efficient manner.

1.2 Performance prediction of engine exhaust systems

The aerodynamic design of the housing components used in the installation of a civil gas-turbine aero-engine, requires the development of an accurate performance prediction and accounting methodology. The engine housing components, such as the intake, bypass and core ducts, and exhaust nozzles, are frequently not designed by the engine manufacturer. Therefore, it is imperative that an appropriate Thrust-Drag Bookkeeping (TDB) method is employed to break down the overall installed engine performance into the individual performance levels of each housing component [9]. This process allows the identification of the main sources of loss and re-focus the design process accordingly so that the dominant installation loss mechanisms are tracked down and mitigated.

Figure 1 presents a typical axi-symmetric housing geometry for a notional turbofan engine with separate-jet exhausts. The aerodynamic performance of the exhaust system is key in TDB. The internal pressure and viscous drag components within the bypass and core nozzle walls can be substantial sources of thrust loss. For example, the reduction in F_G due to losses associated with the performance of the exhaust system can be of the order of 1.5–2.0% relative to the case of fully-expanded ideal flow [10]. In TDB, the actual duct and nozzle performance is related to that of an ideal nozzle through the definition of the non-dimensional discharge and velocity coefficients, C_D and C_V, respectively [11]. An ideal exhaust nozzle is assumed to operate under the premise of one-dimensional (1D) isentropic flow expanded to ambient static pressure [12]. The actual exhaust system performance has been traditionally determined by a combination of small-scale [13, 14] and full-scale model testing [7].

The advent of Computational Fluid Dynamics (CFD) during the past two decades has rendered it a reliable and useful performance prediction tool for the aerodynamic analysis of exhaust nozzles [11, 15–20]. The associated flow phenomena observed in the vicinity of a gas-turbine engine exhaust system can be quite complex. These include, among others, boundary and shear layers interacting with expansion and shock waves. This inherent aerodynamic complexity renders the accurate determination of exhaust nozzle performance a challenge for CFD analysis. Early CFD studies conducted by Malecki and Lord [11] showed that for three-dimensional (3D) exhaust nozzle configurations, the predictive accuracy in terms of C_V can be in the range of 0.5–1.0%. However, with respect to simpler two-dimensional (2D) axi-symmetric cases, the expected accuracy can be of the order of 0.1%. More recent investigations carried out by Zhang *et al.* [15, 16] showed that, for single-stream, axi-symmetric, conical nozzles, the agreement between CFD results and test data can be of the order of 0.2% and 0.5% for C_D and C_V, respectively. However, Zhang *et al.* attributed the quoted percentage differences predominantly to the uncertainty of the experimental data, rather than physical accuracy of the employed CFD approach.

1.3 Scope of present work

In light of the preceding discussion, it is understood that the aerodynamic performance of the bypass exhaust system is key to the success of future large turbofan engines. Therefore, it is essential that the design of the bypass duct, nozzle, and post-exit components is tackled at an early stage of the engine design process. This entails the systematic exploration of the design space governing the aerodynamic behavior of the exhaust system. However, a methodical approach for the parametric geometry definition, aerodynamic analysis, and meticulous examination of separate-jet exhaust systems has not

been reported to date in the existing literature. Furthermore, the impact of future engine cycles incorporating higher values of BPR and lower FPR on exhaust system design, has not been previously investigated.

Within this context, this paper aims to develop an integrated approach which targets the aerodynamic design of separate-jet exhausts for future gas-turbine aero-engines. The proposed method has to be able to identify, quantify, and correlate the fundamental mechanisms that govern the aerodynamic behavior of separate-jet systems for any specified engine cycle. The specific objectives of this work can be outlined as follows:

- To derive an analytical formulation for the parametric geometry definition of separate-jet exhaust systems employed in civil gas-turbine aero-engines
- To establish a modeling approach capable of predicting the aerodynamic performance of the bypass duct, nozzle, and post-exit components of an exhaust system
- To develop an integrated framework for the systematic exploration of the design space that encompasses the aerodynamic performance of separate-jet exhaust systems
- To explore the associated design space for to two civil aero-engine configurations representative of current and future design architectures, respectively

The methodology developed in this paper is broadly arranged as follows; A mathematical method is developed based on Class-Shape Transformation (CST) functions [21, 22] for the geometric design of axi-symmetric engine architectures with separate-jet exhausts. The developed approach inherits the intuitiveness and flexibility of Qin's airfoil parameterization method [23] and extends its applicability to the parametric geometry definition of exhaust ducts and nozzles. The end-result is a compact mathematical model that allows the parametric geometry definition of separate-jet exhausts, based on the required flow capacities. The developed approach is coupled with an automated mesh generation [24] and a Reynolds Averaged Navier–Stokes (RANS) flow-field solution method [25], thus forming an integrated aerodynamic design tool.

The employed CFD approach is initially validated against experimental measurements conducted on a small-scale Turbine Powered Simulator (TPS) nacelle. A comprehensive and cost-effective Design Space Exploration (DSE) method has been structured and coupled with the developed design approach. The combined formulation is applied to explore the design space for two civil aero-engines, representative of current and future large turbofan engines, respectively. The sensitivity of the exhaust systems' performance to changes in the associated design parameters is assessed. Furthermore, the inter-relationship between the exhaust systems' performance metrics of interest is thoroughly quantified and presented. The proposed method enables to quantify and correlate the aerodynamic behavior of separate-jet exhaust systems for any specified engine cycle. Therefore, it constitutes an enabling technology towards identifying the fundamental aerodynamic mechanisms that govern the aerodynamic performance of current and future civil turbofan engines.

2 Numerical approach

2.1 Methodology overview

An integrated tool has been developed for the aerodynamic design and analysis of separate-jet exhaust nozzles. This tool has been named GEMINI (**G**eometric **E**ngine **M**odeler **I**ncluding **N**ozzle **I**nstallation). GEMINI encompasses a generic design approach that is applicable to a wide-range of civil aero-engines. It is able to design separate-jet exhaust systems for any designated engine cycle combined with a prescribed set of key engine hard-points. Figure 2 presents an illustration of the implemented software architecture. The developed method comprises a series of fundamental modeling methods applicable to; engine performance simulation [26], exhaust-nozzle geometry parameterization [21–23], and viscous-compressible flow solution [24, 25].

A designated set of thermodynamic cycle and geometric design parameters is initially defined. The computational method initiates by analyzing the engine cycle at Design Point (DP) and Off-Design (OD) conditions. Engine performance simulation is carried out for a user-specified number of operating points within the operational envelope. The cycle analysis is carried out using the zero-dimensional (0D) aero-thermal approach (Turbomatch) described by Macmillan [26]. This process sizes the bypass and core exhaust nozzles in terms of flow capacity requirements. Furthermore, it provides a first-order indication of the averaged aero-thermal flow properties at the inlet and exit stations of the bypass and core exhaust ducts and nozzles (Fig. 1).

Having established the required flow-capacities, an inverse design approach is employed to obtain a 2D axi-symmetric representation of the bypass and core exhaust aerolines. An example of the 2D axi-symmetric engine geometry produced by GEMINI is shown in Fig. 1. GEMINI has been computationally coupled with an automatic mesh generation tool [24] applicable to 2D axi-symmetric engine geometries with separate-jet exhausts. Thus, among others, GEMINI automatically establishes the computational domain upon which the viscous compressible flow-field can be resolved using a commercial solver [25]. After obtaining a converged CFD solution, the numerical results are automatically post-processed. This procedure determines the bypass and core nozzle discharge coefficients, C_D^{Bypass} and C_D^{Core}, respectively, as well as the overall exhaust system velocity coefficient $C_V^{Overall}$. A detailed description of the individual numerical methods within GEMINI is provided within this section.

2.2 Engine performance simulation (Turbomatch)

The engine performance model (Turbomatch) used for the present work has been developed and refined at Cranfield University over a number of decades [26]. Turbomatch is based on zero-dimensional aero-thermal analysis employing discrete component maps. The employed method essentially solves for the mass and energy balance between the various engine components. Turbomatch has been previously deployed in several studies available in the existing literature for the prediction of DP, OD, and transient performance of gas turbine engines [27, 28]. For the scope of the present work, the engine is assumed to be operating exclusively at steady-state conditions.

2.3 Parametric geometry definition of exhaust nozzles

An analytical approach has been developed for the parametric geometry definition of exhaust systems based on Kulfan's CST functions [21, 22]. The proposed method inherits the intuitiveness of Qin's CST variation [23] and extends its applicability to the parametric representation of exhaust ducts and nozzles. The general form to express a CST function $y(x)$ in the normalized Cartesian space $x \in (0, 1)$ can be written as follows:

$$y(x) = C_{N_2}^{N_1}(x) \cdot S(x) + x \cdot y_{offset}, \quad x \in (0, 1) \tag{1}$$

where $x = \dfrac{X}{L}$ and $y = \dfrac{Y}{L}$ are the normalized independent and dependent coordinates, respectively, whilst L denotes the axial scale. The individual terms in Eq. (1) are defined as follows:

$$C_{N_2}^{N_1}(x) = x^{N_1} \cdot (1-x)^{N_2}, \quad x \in (0, 1) \tag{2a}$$

$$S(x) = \sum_{r=0}^{n} \{A_r K_{r,n} x^r (1-x)^{n-r}\}, \quad x \in (0, 1) \tag{2b}$$

$$K_{r,n} = \frac{n!}{r!(n-r)!} \tag{2c}$$

where $C_{N_2}^{N_1}(x)$ is the class function and $S(x)$ is the shape function. The terms $K_{r,n}$ denote the binomial coefficients whilst y_{offset} signifies the imposed offset in the normal direction between the curve's end-points in the non-dimensional Cartesian space.

It can be observed by inspecting Eq. (2b) that the shape function $S(x)$ corresponds to the nth order Bernstein polynomial $BP_n = \sum_{r=0}^{n} \{K_{r,n} x^r (1-x)^{n-r}\}$ with different weights A_r, $r = 0, ...n$ applied to the associated binomial coefficients $K_{r,n}$. The individual terms $\{K_{r,n} x^r (1-x)^{n-r}\}$, $r = 0, ...n$ that BP_n consists of, are illustrated in Fig. 3 for $n = 8$. When no weighting is applied to the binomial terms ($A_r = 0$, $r = 0, ...n$), the outline of the shape function $S(x)$ (Eq. (2b)) is that of a horizontal straight line with $S(x) = BP_n = 1$. Therefore, the weighting coefficients $A_r, r = 0, ...n$ can be used to alter the outline of $S(x)$ accordingly.

Kulfan [21, 22] showed that the employed class function (Eq. (2a)) is capable of representing a wide range of geometric types. For an airfoil with a round nose and an aft trailing edge, the parameters N_1 and N_2 correspond to 0.5 and 1.0, respectively. Within this work, it has been found that the most appropriate values for N_1 and N_2, are those that give a class function equal to unity $C_{N_2}^{N_1}(x) = 1.0$, them being $N_1 = N_2 = 0$. This choice enables mathematical simplicity and allows the derivation of the proposed parameterization approach in analytical form. Furthermore, it can be shown that for $C_{N_2}^{N_1}(x) = 1.0$, satisfying the end-point boundary conditions $y(0) = 0$ and $y(1) = y_{offset}$, results in $A_0 = A_n = 0$. With these provisions,

Eq. (1) along with its first and second derivatives with respect to x, can be written as:

$$y(x) = \sum_{r=1}^{n-1} \{A_r K_{r,n} H_{r,n}(x)\} + x \cdot y_{offset}, \quad x \in (0,1) \tag{3a}$$

$$y'(x) = \sum_{r=1}^{n-1} \{A_r K_{r,n} \Theta_{r,n}(x)\} + y_{offset}, \quad x \in (0,1) \tag{3b}$$

$$y''(x) = \sum_{r=1}^{n-1} \{A_r K_{r,n} E_{r,n}(x)\}, \quad x \in (0,1) \tag{3c}$$

where $H_{r,n}(x)$, $\Theta_{r,n}(x)$, and $E_{r,n}(x)$ are spatial functions that have been derived in closed form as shown below:

$$H_{r,n}(x) = x^r(1-x)^{n-r} \tag{4a}$$

$$\Theta_{r,n}(x) = r(x^{r-1})(1-x)^{n-r} - x^r(n-r)(1-x)^{n-r-1} \tag{4b}$$

$$E_{r,n}(x) = r(r-1)x^{r-2}(1-x)^{n-r} - 2rx^{r-1}(n-r)(1-x)^{n-r-1} + x^r(n-r)(n-r-1)(1-x)^{n-r-2} \tag{4c}$$

Due to their exponential nature, Eqs. (4a–4c) may exhibit singular behavior at the limits of the independent variable x. Therefore, it is recommended to set the boundaries of x to be asymptotically equal to the associated limiting values $x \in (0,1)$, as determined by machine accuracy. The full-scale geometry in the dimensional Cartesian space can be expressed in parametric form as a function of the independent variable x as follows:

$$X(x) = X_{initial} + L \cdot x \quad x \in (0,1) \tag{5a}$$

$$Y(x) = Y_{initial} + L \cdot y(x) \quad x \in (0,1) \tag{5b}$$

where $X_{initial}$, $Y_{initial}$ are used to translate the derived full-scale curves within the dimensional geometric space. The Cartesian coordinates $X(x)$, $Y(x)$ in Eqs. (5a–5b) can be interchanged with their reciprocal coordinates in the cylindrical system $X(x)$, $R(x)$ to describe the geometry of an axi-symmetric body.

The formulation described above allows the reduction of the bypass as well as core duct and nozzle aerolines to a set of analytical expressions. These can be derived as sole functions of design parameters employed in standard industry practice. Figure 4 presents an illustrative example of the parameters employed in this paper for the geometric representation of an exhaust system. For the purpose of this work, the overall configuration is divided in two components; (a) the upstream duct and (b) the exhaust nozzle. Each component consists of an inner and an outer aeroline. The upstream duct extends axially from the designated inlet plane up to the nozzle Charging Plane (CP) (Fig. 4(a)). The CP is positioned axially at the location where the radius of the inner nozzle aeroline is maximized. The nozzle is positioned aft of the CP and terminates at the

prescribed exit plane (Fig. 4(b)).

The design of the duct is carried out by direct specification of the geometric properties required for a set of designated control-points. These are illustrated in Fig. 4(a) in dashed circles. The controlled geometric properties include radial position R, aeroline slope θ, and curvature radius R_{curve}. The duct inlet hade angles $\theta_{in/out}^{hade}$ are also specified. The geometry of the downstream exhaust nozzle is obtained through prescribing a set of standard design parameters. These include; CP to nozzle exit area ratio $A_{ratio} = \dfrac{A_{CP}}{A_{exit}}$, nozzle length ratio $k_{len} = \dfrac{L_{nozzle}}{h_2}$, CP radial offset R_{CP}^{offset}, aeroline curvature and slope at the nozzle CP location, $R_{curve}^{in/out}$ and θ_{CP}^{out}, respectively, as well as outlet angles $\theta_{in/out}^{nozzle}$.

In terms of nozzle design, the developed method initializes at the nozzle exit plane using as input the known geometric throat area required for a computed flow capacity. The nozzle throat is located at the exit plane for a convergent nozzle. For convergent-divergent nozzles (con-di) an effective con-di ratio is defined, therefore moving the nozzle throat slightly upstream relative to the exit plane. Application of the rolling-ball area estimation method [29] to the nozzle exit plane and upstream CP, results in a series of control points that satisfy the prescribed design parameters. These are shown in Fig. 4(b) in dashed circled lines.

Having defined a series of control points where geometric information is available, a set of spatial Boundary Conditions (BCs) is established for the design of the upstream duct and exhaust nozzle (Fig. 4). Transformation of the imposed BCs in the normalized parametric space $(x, y(x))$ and subsequent application through Eqs. (3a–3c), allows to derive a $(n-1) \times (n-1)$ linear system of equations. The symbol n denotes the order of Bernstein's polynomial required to establish a unique mathematical representation. This is determined by the number of geometric constraints regulating the size of the linear system along with the number of unknowns. Solution of the derived system results in a unique combination of weighting coefficients A_r, $r = 1, \ldots n-1$. These correspond to a parametric geometry representation which uniquely satisfies the imposed BCs. Subsequent application of Eqs. (5a–5b) provides the final geometry for each component.

2.4 CFD domain and boundary conditions

Figure 5 presents the computational domain established for solving the RANS flow equations applied to the geometry of 2D axi-symmetric engines. The free-stream conditions at infinity are modeled using a pressure far-field boundary boundary condition. The free-stream conditions are specified in terms of static pressure P_{st} and temperature T_{st}, as well as Mach number M. The overall size of the domain D_{domain} is defined as a function of the maximum nacelle diameter D_{max} using a scaling factor D_f. For the purpose of this work D_f was set to 150 in accordance with the outcome of a domain sensitivity analysis which showed that nozzle performance was not affected by domain size for $D_f \geq 150$.

The established domain includes the engine intake to account for the effect of mass flow capture ratio on the nacelle pressure distribution. This is required to adequately capture the static pressure aft of the nacelle after-body, and consequently the effect of free-stream suppression on the aerodynamic performance of the exhaust system. The fan face is modeled as a pressure-outlet with uniform radial distribution of static pressure P_{st}. The axial locations at the fan and Low-Pressure Turbine (LPT) Outlet Guide Vane (OGVs) exit planes are modeled as pressure-inlets with prescribed radial distributions of total pressure P_0 and total temperature T_0. The boundary conditions at the fan face and aft of the fan and LPT OGVs

are obtained by analyzing the engine cycle [26]. To account for the non-uniformity of the flow at entry to the bypass duct, circumferentially averaged radial profiles of T_0 and P_0 are imposed as boundary conditions at the exit of the fan OGVs. These have been derived using a streamline curvature method applied to the geometry of the fan rotor and downstream OGVs. The domain includes a third nozzle with a prescribed mass-flow ($\dot{m}$), namely the zone 3 vent. The vent is located between the bypass and core nozzles and is effectively used as a separate exhaust.

2.5 Automatic mesh generation and topology definition

An automated structured grid generation process has been implemented using the commercially available meshing software ANSYS ICEM CFD [24]. A multi-block structure applicable to typical axi-symmetric engine geometries with separate-jet exhausts, is initially defined. A series of implemented meshing rules and procedures are subsequently applied, leading to the automatic generation of the computational grid.

It is noted that the boundary-layer blocks throughout the domain are discretized so as to satisfy the condition of having a y^+ value near unity for all wall-adjacent cells. A total of 50 nodes normal to the aeroline surface are employed in the corresponding boundary-blocks. The radially-outward cell-expansion ratio for the boundary-layer nodes is set equal to 1.2. Figure 6(a) illustrates the derived mesh for the overall computational domain, whilst Fig. 6(b) presents a close-up near the engine surfaces.

2.6 Definition of CFD approach

The commercial flow solver ANSYS Fluent [25] has been selected as the current aerodynamic tool. Computations are carried out using a Reynolds-Averaged Navier-Stokes (RANS) numerical approach coupled with a suitable turbulence model. The suitability of various turbulence models in terms of agreement with measured data for the employed mesh topology (Fig. 6) was investigated by Voulgaris [30]. The conclusions drawn in Ref. [30], resulted in the selection of the $k - \omega$ Shear-Stress Transport (SST) turbulence model for the purpose of this work.

The Green-Gauss node based method is used for computation of the flow-field gradients. A second-order accurate upwind scheme is employed for the spatial discretization of the flow-field variables along with the turbulent kinetic energy k and specific dissipation rate ω. Thermal conductivity (κ) is computed according to kinetic theory. Variable gas properties are employed using an 8th order polynomial expression for the calculation of specific heat capacity (C_p) as a function of static temperature [2]. Sutherland's law is used for the calculation of dynamic viscosity [25].

2.7 Exhaust system performance accounting

The developed approach focuses on the the performance metrics established for exhaust nozzles, namely in terms of non-dimensional discharge and velocity coefficients, C_D and C_V, respectively. The discharge coefficient C_D is defined as the ratio of the actual nozzle mass flow over the ideal isentropic value at the nozzle throat area [31]. The ideal nozzle mass flow per unit area at the nozzle throat for prescribed values of inlet total pressure P_0 and total temperature T_0, is computed as

follows:

$$\left(\frac{\dot{m}}{A}\right)_{Ideal} = P_0 \left(\frac{1}{\lambda}\right)^{\frac{1}{\gamma}} \sqrt{\frac{2\gamma}{(\gamma-1)RT_0}\left(1-\left(\frac{1}{\lambda}\right)^{\frac{\gamma-1}{\gamma}}\right)} \tag{6}$$

where $\lambda = \dfrac{P_0}{P_{amb}}$, p_{amb} denotes the ambient static pressure, R is the gas constant for air, and γ is the ratio of specific heats. Concurrently, the ideal fully-expanded exit velocity is given by [31]:

$$V_{Ideal} = \sqrt{\frac{2\gamma RT_0}{(\gamma-1)}\left(1-\left(\frac{1}{\lambda}\right)^{\frac{\gamma-1}{\gamma}}\right)} \tag{7}$$

It is noted that for $\lambda \geq \lambda_{crit} = \left(\dfrac{\gamma+1}{2}\right)^{\frac{\gamma}{\gamma-1}}$, the value of λ_{crit} is used in Eq. (6), while the actual value of λ is still used in Eq. (7).

For a given nozzle throat area A_{throat} ($= A_{exit}$ for a convergent nozzle), the discharge coefficient is defined as follows:

$$C_D = \frac{\dot{m}_{Actual}}{\left(\dfrac{\dot{m}}{A}\right)_{Ideal} \cdot A_{throat}} \tag{8}$$

The values of $\dot{m}_{Actual}$ in Eq. (8) for the bypass and core nozzles are obtained by integrating the axial mass fluxes across their respective entry planes. Within this work, the selected entry planes are at the pressure-inlet locations where the inlet boundary conditions are imposed for each nozzle (Fig. 7). As a result, the quoted bypass and core nozzle discharge coefficients include the total pressure losses occurring in their respective upstream ducts.

The gross propulsive force $F_G^{Exhaust}$ produced by the exhaust system is computed by integrating the axial gauge stream forces across the nozzle entry boundaries, along with the pressure and viscous shear stress terms on all nozzle walls. These include the core cowl and the protruding core plug. This process is illustrated graphically in Fig. 7 and can be expressed as follows:

$$F_G = F_G^{Bypass} + F_G^{Core} + F_G^{Zone3} - \int_{all\ walls}\left((p-p_{amb})\delta_{1,j} - d_{1,j}\right)dA \tag{9}$$

where F_G^{Bypass}, F_G^{Core}, and F_G^{Zone3} are the axial gauge stream forces at the entry planes of the bypass, core, and zone 3 vent exhaust nozzles, respectively. The nozzle entry planes are illustrated in Fig. 7 using blue coloring. The surface integral

$(\int_{all\ walls} \cdots dA)$ in the RHS of Eq. (9) denotes the integration of the gauge static pressure term $(p - p_{amb})$ normal to the wall boundaries denoted by the vector $\delta_{1,j}$ along with the viscous shear-stress terms $d_{1,j}$ across all of the the no-slip nozzle walls. These are signified in Fig. 7 using red color. The subscript $()_{1,j}$ denotes projection of the integrated force terms in the axial direction. Furthermore, it can be noted from Fig. 7 that the wall contribution integral includes a portion of the nacelle afterbody that reaches up to the axial location of the maximum diameter.

The overall velocity coefficient $C_V^{Overall}$ is defined by referring the gross propulsive force $F_G^{Exhaust}$ to the ideal thrust resulting from the fully-expanded jet velocities V_{Ideal}, and the actual mass flows $\dot{m}_{Actual}$ for the bypass, zone 3 vent, and core streams:

$$C_V^{Overall} = \frac{F_G}{\dot{m}_{Actual}^{Bypass} \cdot V_{Ideal}^{Bypass} + \dot{m}_{Actual}^{Core} \cdot V_{Ideal}^{Core} + \dot{m}_{Actual}^{Zone3} \cdot V_{Ideal}^{Zone3}} \tag{10}$$

It can be noted from Eq. (10) that this definition essentially gives $C_V^{Overall} = 1$ in ideal and fully expanded isentropic flow.

3 Results and discussion

3.1 Grid sensitivity analysis

To establish a robust and theoretically sound computational approach, a grid sensitivity analysis has been carried out to identify the dependency of the obtained CFD solutions on the domain dicretization fidelity. The developed CFD approach has been applied for a 2D axi-symmetric engine representative of current large turbofan designs. Numerical predictions have been carried out at DP mid-cruise conditions. The bypass and core nozzle pressure ratios, intake Mass Flow Capture Ratio (MFCR), and free-stream conditions are documented in Table 1. Figure 8 presents the employed engine geometry, a nominal computational mesh, and the predicted Mach number contours. CFD solutions have been obtained for a total of 5 meshes using progressively increasing grid fidelity. A global scaling factor has been applied to the overall mesh density to ensure uniform refinement. The number of cells N_{cell} is equal to approximately 1.21×10^5 for the coarsest mesh reaching up to 1.05×10^6 for the densest mesh. All meshes employed a y^+ value of nearly 1.0.

Figure 9 presents the influence of N_{cell} on the computed values of C_D^{Bypass}, C_D^{Core}, and $C_V^{Overall}$. It can be observed from Figs. 9(a) and (b) that both C_D^{Bypass} and C_D^{Core} exhibit monotonic convergence characteristics for the entire range of N_{cell} investigated. Figure 9(c) shows that $C_V^{Overall}$ also exhibits monotonic behavior for $N_{cell} \geq 2.65 \times 10^5$. However, the response of $C_V^{Overall}$ for highly coarse grids with $N_{cell} < 2.65 \times 10^5$ is non-monotonic. To quantify the error introduced in the obtained CFD solutions due the spatial discretization of the employed domain, the numerical procedure proposed by Celik *et al.* [32] has been applied. The numerical behavior of the developed meshing approach has been assessed through evaluation of the Grid Convergence Index (GCI). To estimate the GCI for the performance metrics of interest, the meshes with 2.65×10^5, 4.76×10^5, and 7.32×10^5 cells in the monotonic region have been selected.

The estimated GCIs for C_D^{Bypass}, C_D^{Core}, and C_V^{Bypass} are of the order of 0.017%, 0.83%, and 0.058%, respectively. The associated flow-field solution using the medium grid is illustrated in Fig. 8(c). The aforementioned values of GCI indicate

the sound numerical behavior of the developed CFD approach. In accordance with the monotonicity observed in Fig. 9 and the computed values of CGI, an overall mesh fidelity with $N_{cell} = 4.76 \times 10^5$ is selected for the purpose of this work. The implemented mesh topology has been further verified and validated by Voulgaris [30] against publicly available experimental data for small-scale separate-jet and single stream exhaust nozzles.

3.2 Validation of employed CFD approach

Having evaluated the numerical behavior of the employed CFD approach, an appropriate validation exercise has been carried out to assess the proposed method's physical accuracy. The developed tool has been applied to investigate the aerodynamic behavior of an experimental exhaust test apparatus described in a publicly available case study [33, 34]. Experiments were conducted on a Turbine Powered Simulator (TPS) nacelle with separate-jet exhausts in a low-speed wind-tunnel. The various engine components were represented by a two-stage axial fan followed by a three-stage axial turbine. The goal was to compile a representative database to be used for CFD code validation.

Experimental data were collected in terms of bypass nozzle mass flow $\dot{m}_{bypass}$ and gross propulsive force F_G for a set of FPRs ranging from 1.2 to 1.6. Experiments were conducted using a free-stream Mach number of 0.17. A pylon was employed in the bypass exhaust of the test apparatus which resulted in an estimated of area blockage of 8% at the bypass nozzle exit.

The 2D axi-symmetric CFD approach described in this paper was employed to evaluate the aerodynamic performance of the DLR-TPS exhaust system for the test conditions outlined above. An appropriate correction was applied to the obtained CFD data in order to account for the effect of pylon blockage at the bypass nozzle exit. However, any aerodynamic effects related to the 3D nature of the flow, such as skin-friction or flow acceleration induced by the pylon surface, were not captured by the present approach due to the assumption of axi-symmetric flow.

Figure 10 compares numerical predictions with experimental measurements. Results are presented for the normalized bypass nozzle mass flow $\frac{\dot{m}_{bypass}}{\dot{m}_{bypass}^{ref}}$ and overall F_G. $\dot{m}_{bypass}^{ref}$ corresponds to the measured bypass nozzle mass flow for $FPR = 1.2$. Numerical results are presented with (CFD-corr) as well as without accounting for the effect of pylon blockage (CFD). The maximum discrepancies noted between CFD simulations and measured data are of the order 1.92% and 5.40% for the normalized bypass nozzle flow and overall F_G, respectively. These are attributed to the 3D nature of the flow due to the existence of a pylon which is not accounted for by the present CFD approach.

A numerical prediction of the compressible and viscous flow for the TPS apparatus is shown in Fig. 11(a) for $FPR = 1.6$. Computed values of isentropic Mach number $M_{isen.}$ on the inner aerolines of the bypass and core nozzle walls are compared with experimental measurements extracted from Ref. [34] in Fig. 11(b). Good agreement can be generally observed between numerical predictions and measured data. The CFD solution predicts a region of significant flow deceleration in the bypass duct for $x/D_{max} \approx 1.65$ where an aggressive increase in aeroline slope occurs. Although this behavior is in agreement with the experimental data, the minimum $M_{isen.}$ is overpredicted by approximately 10%, as shown in Fig. 11(b). For the specified value of $FPR = 1.6$ the bypass nozzle throat is unchoked. However, the numerical solution indicates the presence of weak shocklets near the nozzle exit as a result of local flow acceleration (Fig. 11(a)). The deviation in $M_{isen.}$ between numerical

predictions and measured data reaches roughly 5-6% on the surfaces of the core cowl and external plug. Overall, it has been shown that the employed CFD approach is able to capture the key features of the flow required for the performance prediction of separate-jet exhausts.

3.3 Design space exploration

To demonstrate the effectiveness and merit of the proposed design approach, the overall method has been implemented within a suitable DSE environment. The inherently nonlinear nature of the problem tackled in this work, in conjunction with the requirement to mitigate the computational cost associated with numerous CFD simulations, have deemed imperative the deployment of a robust method for the Design of Experiment (DOE).

A DOE is a systematic approach to get the maximum amount of system information out of a given number of experiments. Out of the different kinds of DOE available in the literature [35] the Latin Hypercube Design (LHD) algorithm has been selected. The LHD method has been extensively described by Olsson et al. [36]. Following the compilation of a representative design database for a designated engine cycle, the aerodynamic behavior of the exhaust system can be statistically investigated. Within this work, the employed design variables are correlated with the associated performance metrics using Pearson's product moment of correlation [37].

3.3.1 Case study description

The developed methodology has been applied to explore the exhaust system design space for two civil aero-engines. The investigated configurations have been defined in order to be representative of future ($E1$) and current ($E2$) large turbofan architectures. The employed thermodynamic cycles have been been structured using publicly available information [38]. The assumed values of BPR are of the order of 16 and 11 for the future ($E1$) and current ($E2$) engine configuration, in that order. The incorporated cycle parameters in terms of OPR, TET, and component efficiencies have been selected according to the corresponding technology levels using the design guidelines provided in Refs. [2, 39]. Each cycle has been optimized in terms of FPR on the basis of maximizing specific thrust and, concurrently, minimizing overall engine SFC [2].

The 2D axi-symmetric geometries corresponding to the baseline engine models are shown in Fig. 12. The baseline intake, nacelle, and exhaust system geometries have been designed using information found in the public domain combined with informed engineering judgment. Numerical predictions have been carried out at DP mid-cruise conditions considering both engine models. The corresponding bypass and core nozzle pressure ratios, intake MFCR, and free-stream conditions are presented in Table 2. These correspond to the boundary conditions specified for the computations carried out and presented in this section. The associated flow-field solutions for the established baseline engine designs are presented in Figs 13(a) and (b) for the future ($E1$) and current engine architectures ($E2$), respectively. It can be observed that for cruising flight, the bypass exhaust nozzle operates under choked conditions considering both engine models. However, due to the lower values of NPR as shown in Table 2, the core nozzle appears to be unchoked during mid-cruise conditions. This characteristic applies for both engine designs.

3.3.2 Design space definition

To establish a clear definition of the available design space, the bypass exhaust and core afterbody aerolines of the baseline $E1$ and $E2$ engine architectures (Fig. 12), have been reduced to parametric CST representations through Eqs. (5a, 5b). The conceived design space comprises a total of 11 and 12 design variables for the future ($E1$) and current ($E2$) engine configurations, respectively. Figure 14 provides an illustrative description of the parametric geometry definition employed in this paper for the design of separate-jet exhausts. The design space bounds applied for the $E2$ engine (Fig. 12(b)) exhaust design variables are graphically shown. All design variables corresponding to axial or radial dimensions are normalized with a reference length as annotated in Fig. 14. All curvature radii are normalized with CP height h_1. The mathematical definition of each design variable is noted in Fig. 14. A similar parametric design space has been defined for the $E1$ engine.

It can be observed from Fig. 14 that the employed design space comprises variables controlling the design of the bypass duct (y_{bp}^{out}, y_{bp}^{in}), exhaust nozzle (A_{ratio}, κ_{len}^{in}, θ_{CP}^{out}, κ_{CP}^{in}, κ_{CP}^{out}, θ_{nozzle}^{out}), core cowl/afterbody (l_{cr}^{cowl}, θ_{cr}^{cowl}), and zone 3 vent (l_{z3}^{exit}, M_{z3}^{exit}). Figure 14(f) shows how the length of the core cowl l_{cr}^{cowl} can affect the design of the core exhaust for a prescribed LPT OGV plane. For the purpose of this work, the geometry of the core duct and nozzle is adjusted automatically depending on the imposed value of l_{cr}^{cowl} using low-speed contraction design guidelines [40]. It is noted that θ_{nozzle}^{out} is kept constant for the case corresponding to the future engine architecture $E1$. The radial thickness of the nacelle afterbody at the axial location of the bypass nozzle CP is limited to a minimum value to ensure desired manufacturing constraints. The parametric representation of the design space shown in Fig. 14 demonstrates the intuitiveness and flexibility of the proposed approach to represent and manipulate the geometry of separate-jet exhaust systems.

3.3.3 Preliminary statistical analysis

After establishing a thorough representation of the available design space, the developed approach was deployed to investigate the aerodynamic behavior of both engine exhaust systems throughout their domains. Each design space was discretized with the deployment of the implemented LHD method. A database containing approximately 360 exhaust geometries was compiled for each engine using CFD simulations. The correlation between the imposed design variables and the associated performance metrics was subsequently investigated. The objective was to identify the dominant variables and aerodynamic mechanisms that influence the performance of the exhaust system considering both engines.

Table 3 presents a preliminary statistical analysis applied to the obtained DOE results for both engine configurations. Results are presented for the percentage range $R(\%)$ and standard deviation (σ) calculated for each metric. The term NPR_{Zone3} corresponds to the total to static pressure ratio required to drive the vent exhaust $\left(\dfrac{P_0^{inlet}}{P_{st}^{amb}} \right)^{Zone3}$. It is reminded that the vent is modeled as a prescribed mass-flow inlet. Therefore, the required P_0 at the nozzle entry is dependent upon the exit static pressure which is affected by the fan stream suppression effect.

With respect to the future engine design $E1$, a percentage range of approximately 1.7% and 0.35% is observed for C_D^{Bypass} and $C_V^{Overall}$, respectively. Their combined effect results in an even larger variation of F_G reaching approximately 2.9%. A significantly larger range is observed for C_D^{Core} which reaches roughly 23%. It is reminded that core nozzle operates under unchoked conditions, as shown in Fig. 13(a). As a result, for a specified inlet total pressure, the core nozzle mass flow and

discharge coefficient C_D^{Core} are both highly dependent on the exit static pressure. Therefore, the large $R(\%)$ noted in Table 3 for C_D^{Core} is attributed to the strong influence of the core cowl design (Fig. 14(f)) on the static pressure field at the core nozzle exit. With respect to NPR_{Zone3}, the noted $R(\%)$ reaches 34%. This is also mainly due to the static pressure disturbances along the axial direction of the transonic core cowl that affect the unchoked vent exhaust. The transonic flow-field conditions over the engine core afterbody are illustrated in Fig. 13(a).

Regarding the $E2$ engine architecture, a percentage range of the order of 6.2% and 0.87% is noted for C_D^{Bypass} and $C_V^{Overall}$, respectively. The noted values of $R(\%)$ are larger compared to those observed for the future design $E1$. This indicates that the non-dimensional exhaust performance of the $E2$ engine is more responsive to design modifications compared to the future configuration $E1$. This behavior is attributed to two main factors; Firstly, the $E2$ design has a lower BPR and higher NPR_{Bypass} compared to $E1$. This results in a strong, complex, and sensitive shock-pattern on the core afterbody as shown in Fig. 13(b). The sensitivity of the observed flow topology to core cowl design adjustments (Figs. 14(f) and (g)) is reflected predominantly in the larger variation of $C_V^{Overall}$. This is also evident in the percentage range observed for NPR_{Zone3}. The pressure ratio required to drive the unchoked vent is largely influenced by the static pressure distribution on the transonic core cowl as the vent exit location l_{z3}^{exit} and Mach number M_{z3}^{exit} vary during the DOE process (Figs. 14(g) and (h)). Secondly, the design space defined for the $E2$ engine includes the bypass nozzle outer line exit angle θ_{out}^{nozzle}, as shown in Fig. 14(f). This design variable affects the area distribution of the bypass nozzle and can implicitly apply an effective con-di ratio. This modification can alter the aerodynamic performance of the exhaust nozzle, mainly in terms of C_D^{bypass}. This constitutes an additional Degree of Freedom (DOF) that is omitted in the design space of the $E1$ engine.

Furthermore, it can be noticed that the standard deviation (σ) of C_D^{Bypass} is roughly an order of magnitude larger compared to that observed for $C_V^{Overall}$. This behavior applies for both engine architectures, indicating a significantly higher dispersion for the obtained values for C_D^{Bypass}. This higher dispersion indicates the larger sensitivity of C_D^{Bypass} to exhaust design adjustments in comparison to $C_V^{Overall}$. The results presented in table 3 suggest that the computed values of $C_V^{Overall}$ are densely concentrated around their mean values while C_D^{Bypass} appears to exhibit a more scattered distribution. This is attributed to the employed definition of $C_V^{Overall}$ where normalization is carried out on the basis of the actual exhaust nozzle mass flow as described by Eq. (10). The employed definition essentially renders $C_V^{Overall}$ independent of C_D^{Bypass} to first-order, thus leading to a smaller σ for $C_V^{Overall}$.

3.3.4 Assessment of apparent design space linearity

Figures 15 and 16 present the estimated linear correlation coefficients, also known as Pearson's product-moment of correlation [37], for the performance metrics of interest. Computational results are presented for the $E1$ and the $E2$ engine in Figs. 15 and 16, respectively. The principal linear correlation coefficients indicate the amount and type of average dependency between two specified parameters. A correlation coefficient can range from -1 to 1. A positive and a negative nonzero value will indicate a direct and an indirect correlation, respectively.

Figure 15(a) presents the computed correlation for C_D^{Bypass} and $C_V^{Overall}$ for the future $E1$ engine. Considerable data scatter can be observed. However, the positive slope identified indicates that an improvement in $C_V^{Overall}$ is nominally ac-

companied by an increase in C_D^{Bypass}. The computed value for Pearson's product-moment of correlation is 0.60. However, the observed metric behavior also indicates that it is possible for an exhaust system to exhibit good performance in terms of C_D^{Bypass}, but have poor $C_V^{Overall}$ characteristics. Specifically, a percentage range of approximately 0.35% can be noticed in the variation of $C_V^{Overall}$ at constant C_D^{Bypass} close to its optimum value.

A similar behavior is observed in in Fig. 16(a) where the correlation between C_D^{Bypass} and $C_V^{Overall}$ is presented for the current $E2$ engine design. However, it can be noticed that the obtained data are more densely concentrated around the mean regression line. The corresponding value of the linear correlation coefficient is of the order 0.79. A similar percentage range (0.3%) is observed for $C_V^{Overall}$ close to the design region of optimum C_D^{Bypass}. Overall, the results confirm that an exhaust system that is optimum in terms of $C_V^{Overall}$ will also be accompanied by C_D^{Bypass} performance close to optimum value. The opposite statement does not hold true for either engine architecture.

Figures 15 and 16(b) show that there is a strong correlation between C_D^{Bypass} and F_N with respect to both engine configurations. The corresponding correlation coefficients are of the order of 0.86 and 0.88 for the $E1$ and $E2$ engine, respectively. This is attributed predominantly to the increased engine mass flow associated with better performance in terms of C_D^{Bypass}. Another important element that influences the correlation is the effect of $C_V^{Overall}$ which is implicit in the results shown in Figs. 15 and 16(b). Specifically, with respect to the $E1$ engine architecture, Fig. 15(b) shows at a value of C_D^{Bypass} close to optimum, the previously observed percentage range of 0.35% in $C_V^{Overall}$, results in a variation of F_N of the order of 5% relative to it nominal value. However, as regards the $E2$ engine, Fig. 16(b) shows that the associated percentage range in F_N is roughly 2.5%, despite the fact that the variation in $C_V^{Overall}$ is close to 0.3%. The observed behavior suggests that the exchange rates between F_N and exhaust $C_V^{Overall}$ for future turbofan engines, can be almost double in magnitude compared to those of current engine architectures.

The correlation between $C_V^{Overall}$ and F_N is shown in Figs. 15 and 16(c) for the $E1$ and $E2$ engine, respectively. The associated Pearson indices are of the order of 0.71 and 0.86. The results show that F_N is strongly dependent on $C_V^{Overall}$, as expected. However, the computed correlations are not completely linear. This is due to the implicit variations in C_D^{Bypass}. F_N is affected significantly by both C_D^{Bypass} and $C_V^{Overall}$. However, there is an apparent non-linearity in correlating the behavior of C_D^{Bypass} and $C_V^{Overall}$ as shown in Figs. 15 and 16(a). This is especially in the low C_D^{Bypass} design region of the $E1$ engine (Fig. 15(a)) where significant scatter is observed. The observed non-linearity can implicitly propagate to influence the dependence of F_N on $C_V^{Overall}$, especially in the low C_D^{Bypass} region (Fig.15(c)).

Figure 17 presents the associated correlation matrices obtained through systematic exploration of the design space corresponding to both engine architectures. The results are presented in the form of Hinton diagrams. Hinton diagrams can be useful in visualizing numerical data in linear algebra, particularly considering weighting or correlation matrices. The presented illustrations demonstrate the distribution of Pearson's product-moment of correlation between the available design variables (Fig. 14) and the performance metrics of interest (Table 3). Results are presented for the $E1$ and $E2$ engine architectures in Figs. 17(a) and (b), respectively. Both correlation matrices have been compiled by consistently applying the process demonstrated in Figs. 15–16 throughout the overall design space.

Figure 17(a) shows that, with respect to the $E1$ engine, the dominant design parameters that affect C_D^{Bypass} are the nozzle

length ratio κ_{len}^{in} (Fig. 14(c)) and the core cowl angle θ_{cr}^{cowl} (Figs. 14(f) and (i)). Specifically, the obtained results suggest that good performance in terms of C_D^{Bypass} requires increased values of length ratio κ_{len}^{in} along with low core cowl angles θ_{cr}^{cowl}. In terms of $C_V^{Overall}$, Fig. 17(a) shows that the dominant design parameter is the outer aeroline slope at the charging plane θ_{CP}^{out} (Fig. 14(d)). The obtained results indicate a positive effect for increased values of θ_{CP}^{out} and vice-versa. The combined influence of C_D^{Bypass} and $C_V^{Overall}$ is also observed in terms of F_G and F_N, which are also strongly affected by κ_{len}^{in}, θ_{cr}^{cowl}, and θ_{CP}^{out}.

A similar behavior can be observed in Fig. 17(b) with respect to exhaust system performance of the $E2$ engine. It can be noticed that the dominant design variables are the same as those identified for the $E1$ engine, namely; κ_{len}^{in}, θ_{cr}^{cowl}, and θ_{CP}^{out}. However, the principal parameter that affects C_D^{Bypass} is θ_{CP}^{out} (Fig. 14(d)) with κ_{len}^{in} (Fig. 14(c)) assuming a secondary role. Thus, although the polarity of the effect of the two variables is the same as noted for the $E1$ engine, their relative impact on C_D^{Bypass} is significantly different. A similar observation applies for $C_V^{Overall}$ where the dominant design parameter is κ_{len}^{in} whilst θ_{CP}^{out} becomes secondary. Furthermore, increasing the core cowl angle θ_{cr}^{cowl} (Figs. 14(f) and (i)) has an adverse effect on both C_D^{Bypass} and $C_V^{Overall}$ with an analogous influence on F_N. It is interesting to note that the computed value for the correlation coefficient that relates F_N to θ_{cr}^{cowl} is roughly -0.62 for both engine architectures. This is attributed to the adverse effect on the core cowl boundary layer that is induced when increasing the afterbody angle beyond the nominal value of 14 degrees.

Figures 17(a) and (b) can be viewed as design guidelines towards improving the aerodynamic performance of separate-jet exhaust systems for designated engine cycles. Figure 18 presents an application example of the design guidelines identified in Fig. 17(a) for the exhaust system of the future engine $E1$. The aerodynamic behavior of the baseline and improved bypass nozzle designs are shown in Figs. 18(a) and (b), respectively.

It can be observed that the baseline design produces a strong normal shock located at approximately $0.5 \times h_2$ downstream of the nozzle exit plane. This strong normal shock generates entropy, limits the exhaust system's capacity, reduces the jet's total pressure and overall F_G. Figure 18(b) shows that this undesirable flow feature has been mitigated by improving the design according to the guidelines presented in Fig. 17(a). This has been achieved by increasing the nozzle length ratio κ_{len}^{in} (Fig. 12(c)) and moving the Low-Pressure (LP) turbine "hump" upstream relative to the baseline exhaust system. This adjustment allows the flow to gradually align itself with the core cowl angle before being exhausted to ambient. As a result, flow acceleration to sonic conditions is achieved predominantly through mean flow area reduction, instead of locally induced acceleration due to aeroline curvature. Furthermore, the value of θ_{CP}^{out} (Fig. 12(d)) has been set equal to it's maximum value which is $0°$. This design arrangement in combination with the horizontal inner aeroline at the CP ($\theta_{CP}^{in} = 0°$), have minimized any radial pressure gradients at the CP prior to any flow turning in the exhaust nozzle.

The combined effect of the aforementioned design adjustments has lead to an improvement in C_D^{Bypass} and $C_V^{overall}$ for the future $E1$ engine of the order of 0.4% and 0.06%, respectively. This has resulted in a F_G increase of approximately 0.45%. Hence, it has been shown that the proposed approach allows to identify effective guidelines for the improved design of separate-jet exhausts with respect to future and current civil aero-engines.

4 Conclusions

An integrated approach has been developed which targets the aerodynamic design of separate-jet exhaust systems for future gas-turbine aero-engines. The overall method is based on a set of fundamental modeling theories applicable to engine performance simulation, parametric geometry definition, and viscous/compressible flow solution. An analytical approach has been developed for the parametric geometry definition of separate-jet exhausts based on CST functions. The proposed formulation inherits the intuitiveness and flexibility of the Qin's CST variation and extends its applicability to the parametric representation of exhaust ducts and nozzles. A suitable aerodynamic modeling approach has been established and validated against publicly available experimental data. The developed design approach has been coupled with a comprehensive formulation for design space exploration. The overall framework has been deployed to investigate the overall design space for to two civil aero-engines representative of current and future architectures, respectively. The sensitivity of the exhaust systems' performance metrics to parametric design adjustments has been assessed. The inter-relationship between exhaust systems' performance metrics of interest has been quantified and presented.

It has been shown that the developed analytical approach is a powerful mathematical tool for the parametric representation and geometric manipulation of separate-jet exhaust systems. It has been demonstrated that the use of correlation matrices in the form of Hinton diagrams can be effective in representing the behavior of the aerodynamic design space for the case of separate-jet exhausts. The proposed approach has been successful in identifying effective guidelines for the improved design of separate-jet exhaust systems. Furthermore, it enables to quantify and correlate the aerodynamic behavior of any separate-jet exhaust system for any specified engine architecture. Therefore, it constitutes an enabling technology towards identifying the fundamental aerodynamic mechanisms that govern the aerodynamic performance of current and future civil turbofan engines.

5 Acknowledgments

References

[1] Epstein, A. H., "Aeropropulsion for Commercial Aviation in the Twenty-First Century and Research Directions Needed," *AIAA Journal*, Vol. 52, (5), May 2014, pp. 901–911.

[2] Walsh, P. and Fletcher, P., *Gas Turbine Performance Engineering*, Blackwell Publishing, 2004.

[3] Kyprianidis, K. G., Grnstedt, T., Ogaji, S. O. T., Pilidis, P., and Singh, R., "Assessment of Future Aero-engine Designs With Intercooled and Intercooled Recuperated Cores," *ASME*, Vol. 133, (1), April 2010, pp. 011701.

[4] Kyprianidis, K. G., Rolt, A. M., and Grnstedt, T., "Multidisciplinary Analysis of a Geared Fan Intercooled Core Aero-Engine," *ASME J. Eng. Gas Turbines and Power*, Vol. 136, (1), January 2013, pp. 011203.

[5] Kyprianidis, K. G. and Rolt, A. M., "On the Optimization of a Geared Fan Intercooled Core Engine Design," *ASME J. Eng. Gas Turbines and Power*, Vol. 137, (4), April 2014, pp. 041201.

[6] Guha, A., "Optimum Fan Pressure Ratio for Bypass Engines with Separate or Mixed Exhaust Streams," *Journal of Propulsion and Power*, Vol. 17, (5), September-October 2001 2001, pp. 1117–1122.

[7] MIDA, S. G., "Guide to In-Flight Thrust Measurement of Turbojets and Fan Engines," Advisory Group for Aerospace Research and Development, AGARD-AG-237, January 1979.

[8] AGARD, "Aerodynamics of Power Plan Installation," Advisory Group for Aerospace Research and Development, AGARD-CP-301, 7 Rue Ancelle 92200 Newilly, Sur Seine, France, May 1981.

[9] Covert, E. E., James, C. R., Kimsey, W. M., Rickey, G. K., and Rooney, E., *Thrust and Drag: Its Prediction and Verification (Progress in Astronautics and Aeronautics Series)*, American Institute of Aeronautics & Astronautics, Reston, VA 20191-4344, 1985.

[10] Dusa, D., Lahti, D., and Berry, D., "Investigation of Subsonic Nacelle Performance Improvement Concept," 18th Joint Propulsion Conference, Cleveland, OH, U.S.A, June 21-23 1982.

[11] Malecki, R. E. and Lord, K., "Aerodynamic Performance of Exhaust Nozzles Derived from CFD Simulation," American Institute for Aeronautics and Astronautics, AIAA-1995-2623, Reston, VA 20191-4344, 1995.

[12] Decher, R. and Tegeler, D. C., "High Accuracy Force Accounting Procedures for Turbo Powered Simulator Testing," American Institute for Aeronautics and Astronautics, AIAA-1975-1324, Reston, VA 20191-4344, 1975.

[13] von Greyr, H. F. and Rossow, C. C., "A Correct Thrust Determination Method for Turbine Powered Simulators In-Wind Tunnel Testing," American Institute for Aeronautics and Astronautics, AIAA-2005-3707, Reston, VA 20191-4344, 2005.

[14] Hughes, C. E., Podboy, G. G., Woodward, R. P., and Jeracki, R. J., "The Effect of Bypass Nozzle Exit Area on Fan Aerodynamic Performance and Noise in a Model Turbofan Simulator," National Aeronautics and Space Administration, TM2013-214029, Glenn Research Center, Cleveland, Ohio, December 2013.

[15] Zhang, Y., Chen, H., Zhang, M., Zhang, M., Li, Z., and Fu, S., "Performance Prediction of Conical Nozzle Using Navier-Stokes Computation," *Journal of Propulsion and Power*, Vol. 31, (1), January-February 2015, pp. 192–203.

[16] Zhang, Y., Chen, H., Fu, S., Zhang, M., and Zhang, M., "Drag Prediction Method of Powered-On Civil Aircraft Based on Thrust-Drag Bookkeping," *Chinese Journal of Aeronautics*, Vol. 28, (4), August 2015, pp. 1023–1033.

[17] Sloan, B., Wang, J., Spence, S., Raghunathan, S., and Riordan, D., "Aerodynamic Performance of a Bypass Engine with Fan Nozzle Exit Area Change by Warped Chevrons," *IMechE Journal of Aerospace Engineering*, Vol. 224, (6), January 2010, pp. 731–743.

[18] Hsiao, E., Su, M. W., and Colehour, J. L., "Navier-Stokes Analysis of a High By-Pass Engine Exhaust System and Plume," American Institute of Aeronautics and Astronautics, AIAA-1997-2282, Reston, VA 20191-4344, 1997.

[19] Speir, D. W. and Blozy, J. T., "Internal Performance Prediction for Advanced Exhaust Systems," *Journal of Aircraft*, Vol. 20, (3), No. 216-221, March 1983.

[20] Abdol-Hamid, K. S., "Commercial Turbofan Engine Exhust Nozzle Flow Analyses," *Journal of Propulsion and Power*, Vol. 9, (3), May 1993, pp. 431–436.

[21] Kulfan, B. M., "Recent Extensions and Applications of the 'CST' Universal Parametric Geometry Representation Method," *Aeronautical Journal*, Vol. 114, (1153), March 2010, pp. 157–176.

[22] Kulfan, B. M., "Universal Parametric Geometry Representation Method," *Journal of Aircraft*, Vol. 45, (1), January-February 2008, pp. 142–158.

[23] Zhu, F. and Qin, N., "Intuitive Class/Shape Function Parameterization for Airfoils," *AIAA Journal*, Vol. 52, (1), January 2014, pp. 17–25.

[24] Ansys Inc., 275 Technology Drive, Canonsburg, PA 15317, *ANSYS ICEM CFD Tutorial Manual*.

[25] Ansys Inc., 275 Technology Drive, Canonsburg, PA 15317, *ANSYS FLUENT User's Guide*.

[26] Macmillan, W. L., *Development of a Module Type Computer Program for the Calculation of Gas Turbine Off Design Performance*, Ph.D. thesis, Department of Power and Propulsion, Cranfield University, 1974.

[27] Li, Y. G., Marinai, L., Gatto, E. L., Pachidis, V., and Pilidis, P., "Multiple-Point Adaptive Performance Simulation Tuned to Aeroengine Test-Bed Data," *Journal of Propulsion and Power*, Vol. 25, (3), 2009, pp. 635–641.

[28] Pachidis, V., Pilidis, P., Marinai, L., and Templalexis, I., "Towards a full two dimensional gas turbine performance simulator," *Aeronautical Journal*, Vol. 111, (1121), 2007, pp. 433–442.

[29] Lee, Y.-S., Ma, Y., and Jegadesh, G., "Rolling-Ball Method and Contour Marching Approach to Identifying Critical Regions for Complex Surface Machining," *Computers in Industry*, Vol. 41, (2), March 2000, pp. 163–180.

[30] Voulgaris, I., *Civil Aircraft Nacelle and Afterbody Aerodynamics*, Master's thesis, Cranfield University, Bedfordshire, UK, MK430AL, August 2014.

[31] Anderson, J. D., *Modern Compressible Flow: With Historical Perspective*, McGraw-Hill Education, Columbus, OH 43218, 3rd ed., 2002.

[32] Celik, I. B., Ghia, U., Roache, P. J., Freitas, C. J., Coleman, H., and Raad, P. E., "Procedure for Estimation and Reporting of Uncertainty Due to Discretization in CFD Applications," *ASME J. Fluids Eng.*, Vol. 130, (7), July 2008, pp. 078001.

[33] Klock, R. and Baumert, W., "A Selection of Experimental Test Cases for the Validation of CFD codes, Volume I," Advisory Group for Aerospace Research and Development, AGARD-AR-303 Vol. 1, 7 RUE ANCELLE, 92200 NEUILLY-SUR-SEINE, FRANCE, August 1994.

[34] Klock, R. and Baumert, W., "A Selection of Experimental Test Cases for the Validation of CFD codes, Volume II," Advisory Group for Aerospace Research and Development, AOARD-AR-303 Vol. 2, 7 RUE ANCELLE, 92200 NEUILLY-SUR-SEINE, FRANCE, August 1994.

[35] Lorenzen, T. and Anderson, V., *Design of Experiments: A No-Name Approach*, CRC Press, Boca Raton, FL 33487, USA, 1993.

[36] Olsson, A., Sandberg, G., and Dahlblom, O., "On Latin hypercube sampling for structural reliability analysis," *Structural Safety*, Vol. 25, No. 1, 2003, pp. 47 – 68.

[37] Hotelling, H., "New Light in the Correlation Coefficient and its Transforms," *Journal of the Royal Statistical Society*, Vol. 15, (2), No. 193-232, 1953.

[38] Gunston, B., *Jane's Aero-engines*, Jane's Information Group, 1996.

[39] Mattingly, J., *Elements of gas turbine propulsion*, No. v. 1 in McGraw-Hill series in mechanical engineering, McGraw-Hill, 1996.

[40] Bell, J. H. and Mehta, R. D., "Contraction Design for Small Low-Speed Wind Tunnels," Stanford University, Department of Aeronautics and Astronautics, NASA CR 182747, April 1988.

List of Figures

List of Tables

Table 1.   Engine operating conditions used for grid dependency analysis

Cycle parameter.	Value	Unit
$\left(\dfrac{P_0^{inlet}}{P_{st}^{amb}}\right)^{Bypass}$	2.8	–
$\left(\dfrac{P_0^{inlet}}{P_{st}^{amb}}\right)^{Core}$	1.4	–
$MFCR^{intake}$	0.6	–
M_∞	0.85	–
Altitude	13106	m

Table 2. Engine operating conditions used for Design Space Exploration

Cycle parameter.	$E1$	$E2$	Unit
$\left(\dfrac{P_0^{inlet}}{P_{st}^{amb}}\right)^{Bypass}$	2.2	2.8	–
$\left(\dfrac{P_0^{inlet}}{P_{st}^{amb}}\right)^{Core}$	1.5	1.4	–
$MFCR^{intake}$	0.7	0.6	–
BPR	16	11	–
M_∞	0.85	0.85	–
Altitude	10668	13106	m
Rated cruise F_N	$\approx$60	$\approx$40	kN

Table 3.   Design space statistical analysis

Metric	Percentage range R (%)	St. deviation (σ)
	$R = \dfrac{\phi_{max} - \phi_{min}}{\phi_{min}}\%$	$\sigma = \sqrt{\dfrac{\sum_{n=1}^{N}(\phi_i - \mu)^2}{N}}$
$E1$ engine		
C_D^{Bypass}	1.7	0.0037
C_D^{Core}	23	0.035
$C_V^{Overall}$	0.35	0.0005
F_G	2.9 (%)	1318 (N)
NPR_{Zone3}	34	0.093
$E2$ engine		
C_D^{Bypass}	6.2	0.011
C_D^{Core}	66	0.077
$C_V^{Overall}$	0.87	0.0014
F_G	8.6 (%)	1795 (N)
NPR_{Zone3}	86	0.17
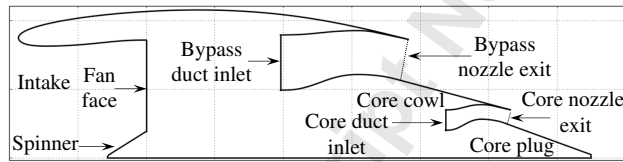
Fig. 1. Notional axi-symmetric housing geometry for a Very-High Bypass Ratio (VHBR) turbofan engine with separate-jet exhausts
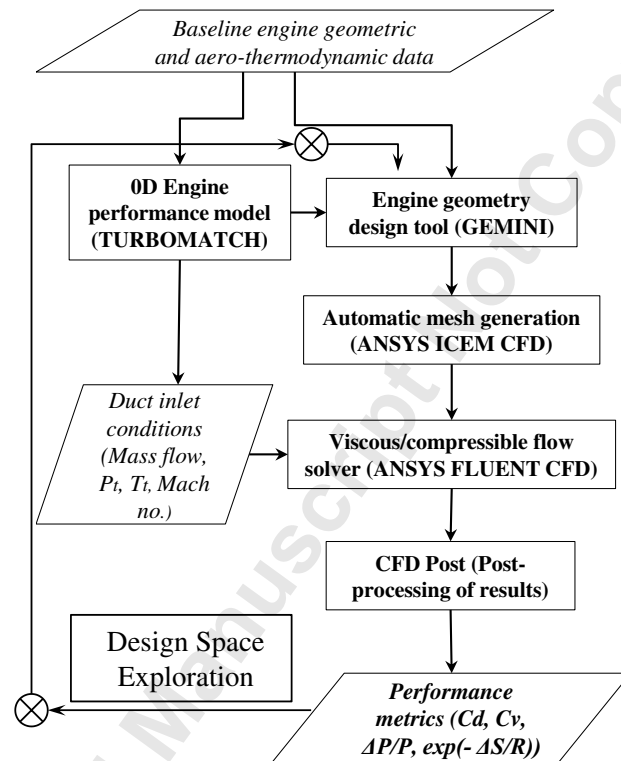
Fig. 2. Upper-level overview of the developed software architecture

$$\sum_{r=0}^{n}\{K_{r,n}x^r(1-x)^{n-r}\} = 1$$
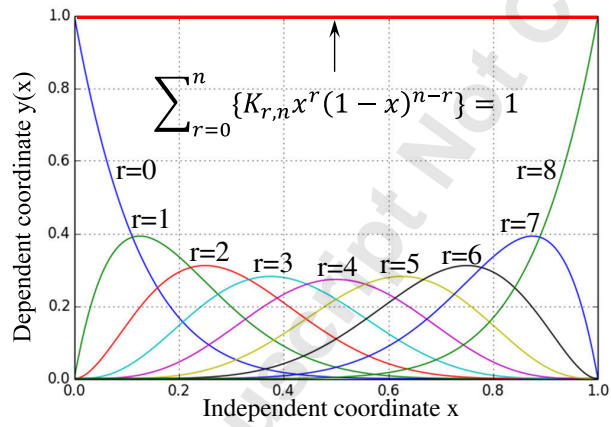
Fig. 3.   Individual terms comprising Bernstein's polynomial for $n = 8$
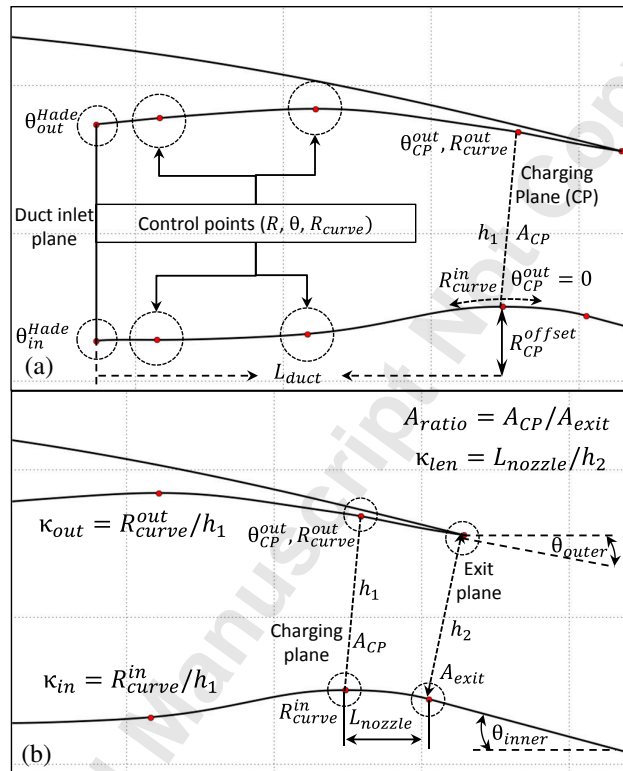
Fig. 4. Employed parameters for the parametric geometry representation of an exhaust system : (a) duct geometry, (b) nozzle geometry
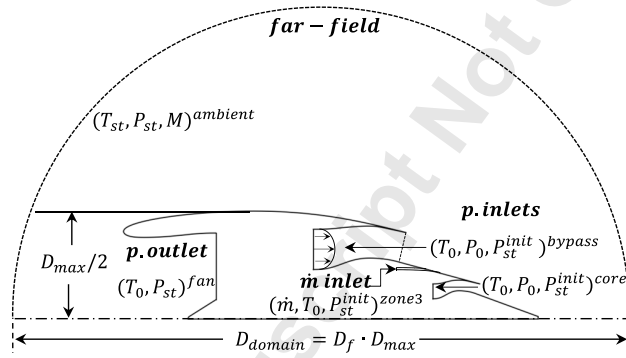
Fig. 5.   Employed CFD domain and boundary conditions
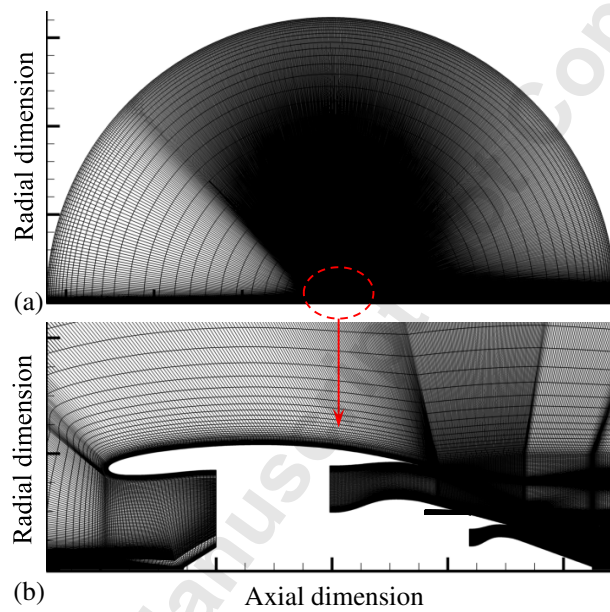
Fig. 6. Mesh generation and topology definition: (a) Overall view of derived computational mesh, (b) Mesh close-up
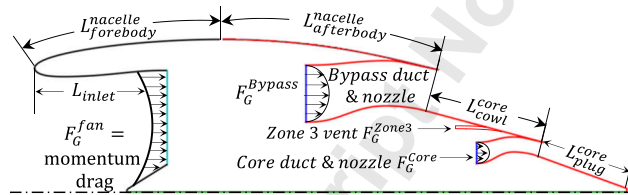
Fig. 7.   Graphical illustration of force accounting for the computation of gross propulsive force $F_G^{exhaust}$
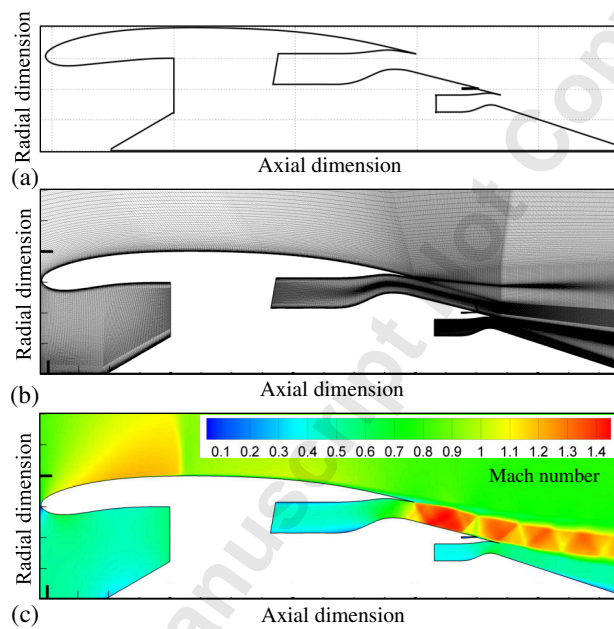
Fig. 8. Engine model used for the grid sensitivity analysis: (a) Model geometry, (b) Computational mesh, $N_{cell} \approx 4.76 \times 10^5$, (c) Mach number contours at mid-cruise conditions, $M_\infty = 0.85, Alt. = 13106.4m$
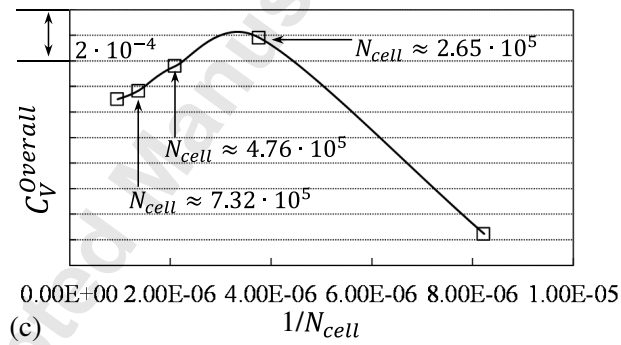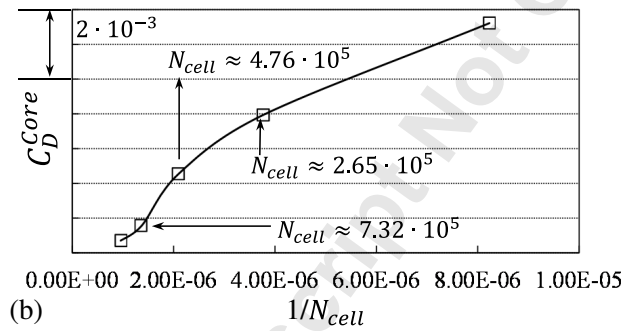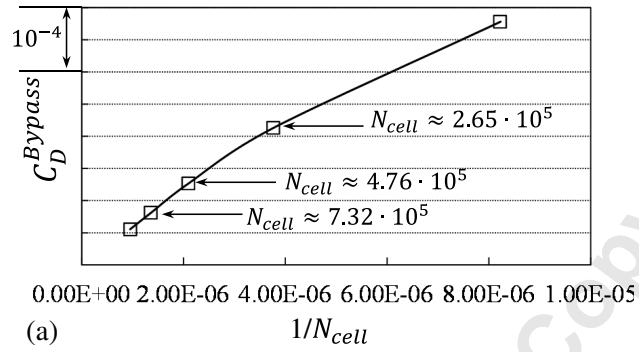
Fig. 9.   Grid sensitivity analysis for the described engine model: (a) Bypass nozzle discharge coefficient C_D^{Bypass}, (b) Core nozzle discharge coefficient C_D^{Core} (c) Overall exhaust velocity coefficient $C_V^{Overall}$
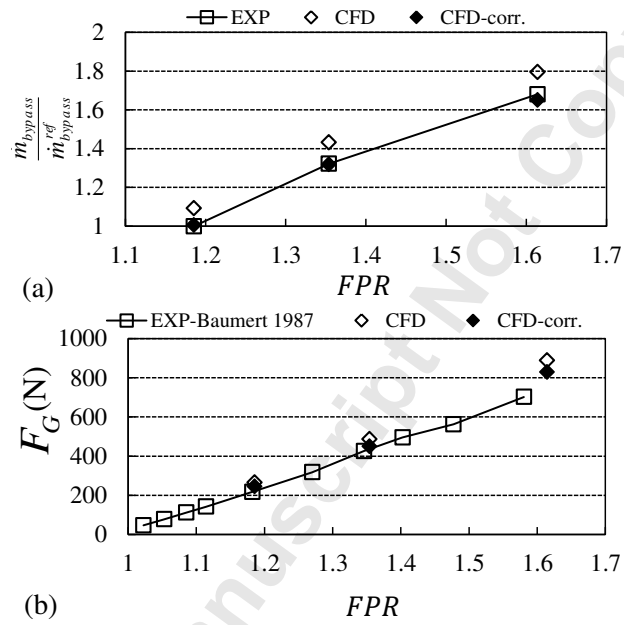
Fig. 10. Comparison of predicted nozzle performance parameters with experimental data reported in Ref. [34]: (a) Normalized bypass nozzle mass flow $\frac{\dot{m}_{bypass}}{\dot{m}_{bypass}^{ref}}$, Gross propulsive force F_G
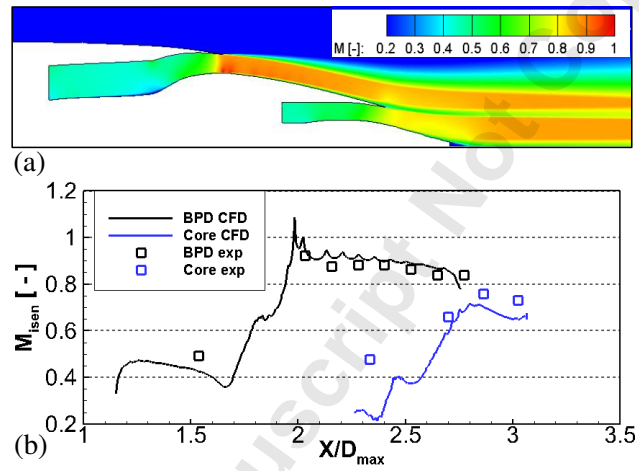
Fig. 11. Model validation: (a) Mach number contours for $FPR = 1.6$, $M_\infty = 0.17$, (b) Isentropic Mach number M_{isen} on the bypass and core nozzle inner walls – comparison with experimental data from Ref. [34]
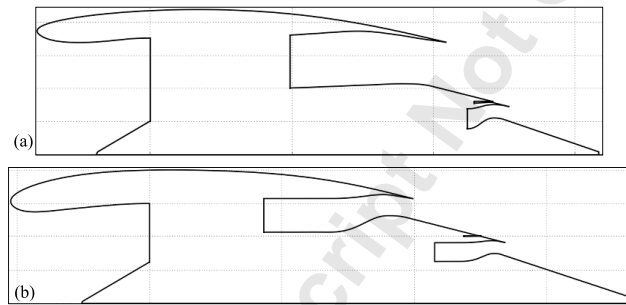
Fig. 12. 2D axi-symmetric geometries of investigated engine architectures: (a) Design representative of future engine architectures ($E1$), (b) Design representative of current engine architectures ($E2$)
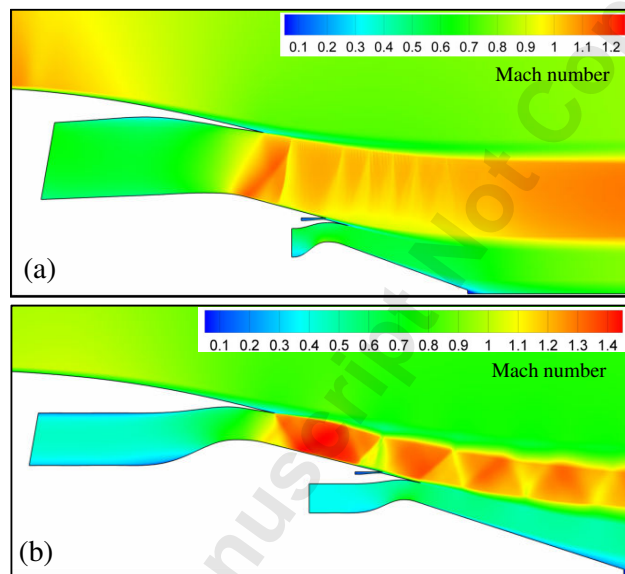
Fig. 13. Mach number contours for the baseline exhaust system designs at DP mid-cruise conditions: (a) Design representative of future engine architectures ($E1$), (b) Design representative of current engine architectures ($E2$)
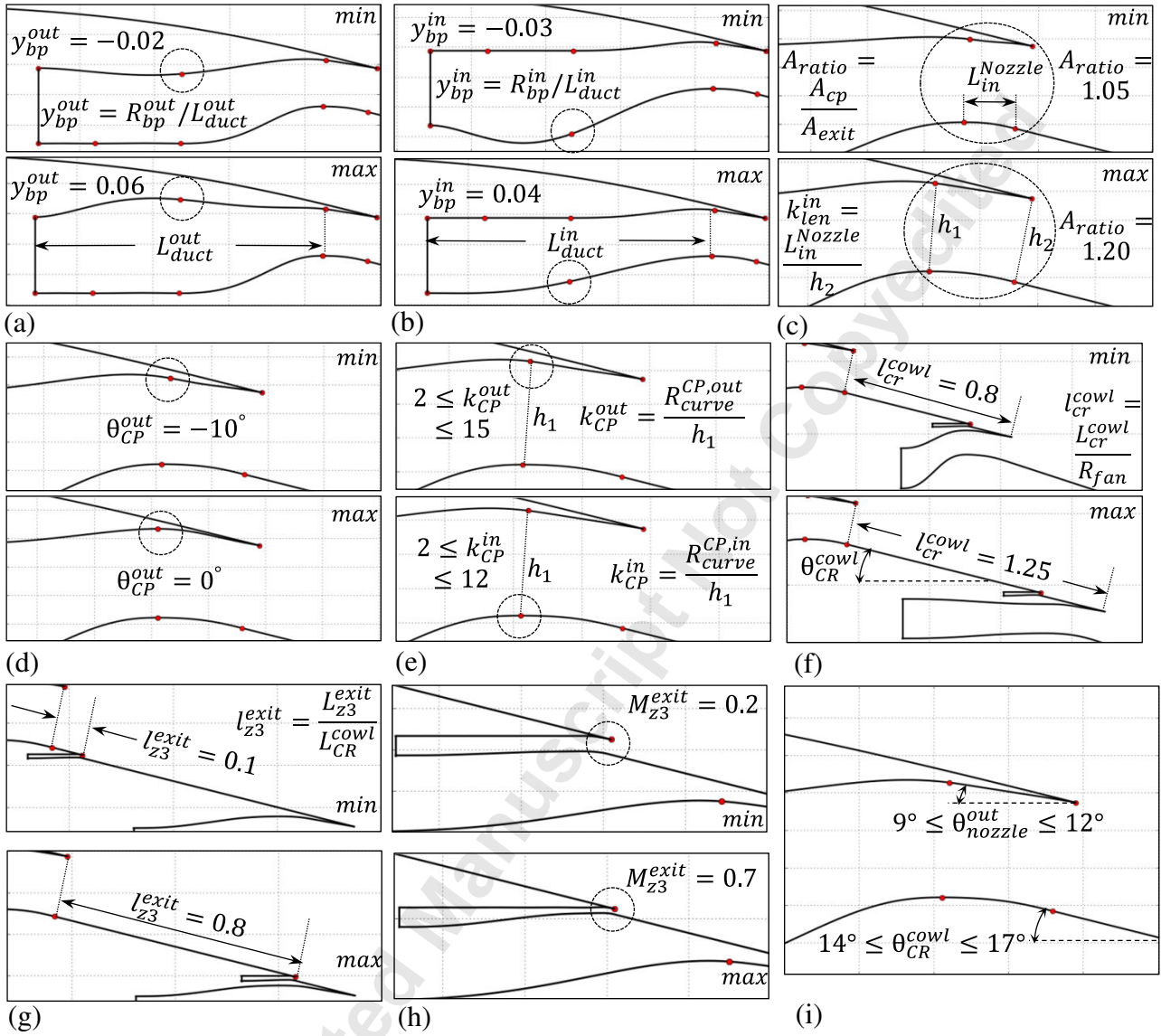
Fig. 14. Design space definition: (a) Bypass duct outer line position $y_{bp}^{out} = \dfrac{R_{bp}^{out}}{L_{duct}^{in}}$, (b) $y_{bp}^{in} = \dfrac{R_{bp}^{in}}{L_{duct}^{in}}$, (c) Nozzle CP to exit area ratio $A_{ratio} = \dfrac{A_{CP}}{A_{exit}}$ and length ratio $\kappa_{len}^{in} = \dfrac{L_{in}^{Nozzle}}{h_2}$, (d) Outer line slope at the CP θ_{CP}^{out}, (e) CP inner/outer curvature radius ratio $\kappa_{CP}^{in/out} = \dfrac{R_{curve}^{CP,in/out}}{h_2}$, (f) Core cowl length $l_{cr}^{cowl} = \dfrac{L_{cr}^{cowl}}{R_{fan}}$, (g) Zone 3 vent exit position $l_{z3}^{exit} = \dfrac{L_{z3}^{exit}}{L_{cr}^{cowl}}$, (h) Zone 3 exit Mach no. M_{z3}^{exit}, (i) Core cowl angle θ_{cr}^{cowl} and outer line angle θ_{nozzle}^{out}
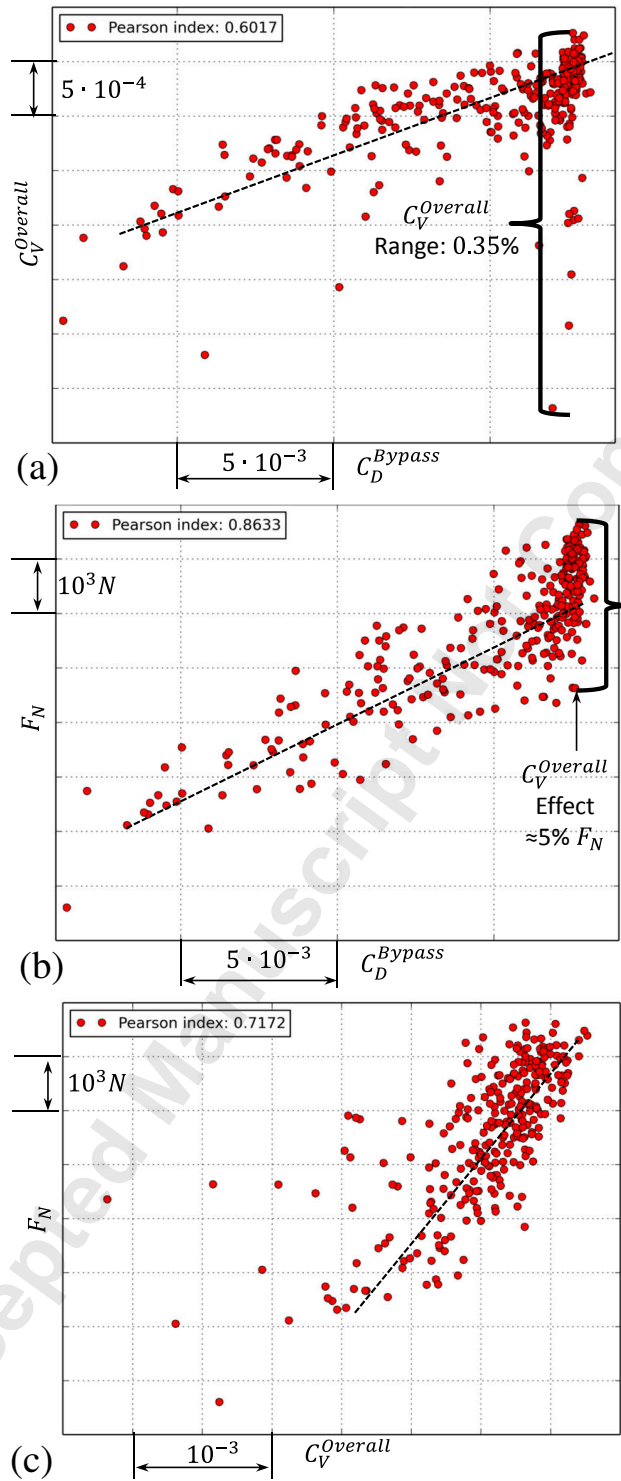
Fig. 15. Correlation of performance metrics for the future $E1$ engine: (a) C_D^{Bypass} and $C_V^{Overall}$, (b) C_D^{Bypass} and F_N, (c) $C_V^{Overall}$ and F_N
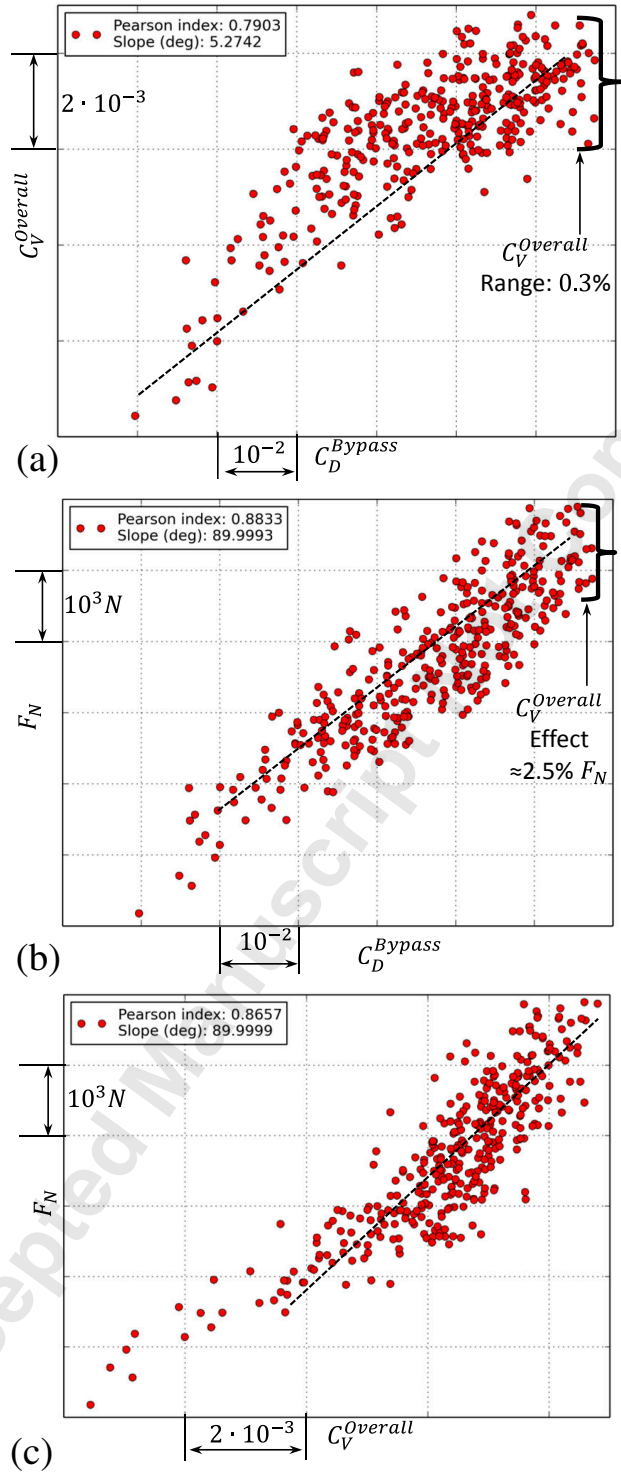
Fig. 16. Correlation of performance metrics for the current $E2$ engine: (a) C_D^{Bypass} and $C_V^{Overall}$, (b) C_D^{Bypass} and F_N, (c) $C_V^{Overall}$ and F_N
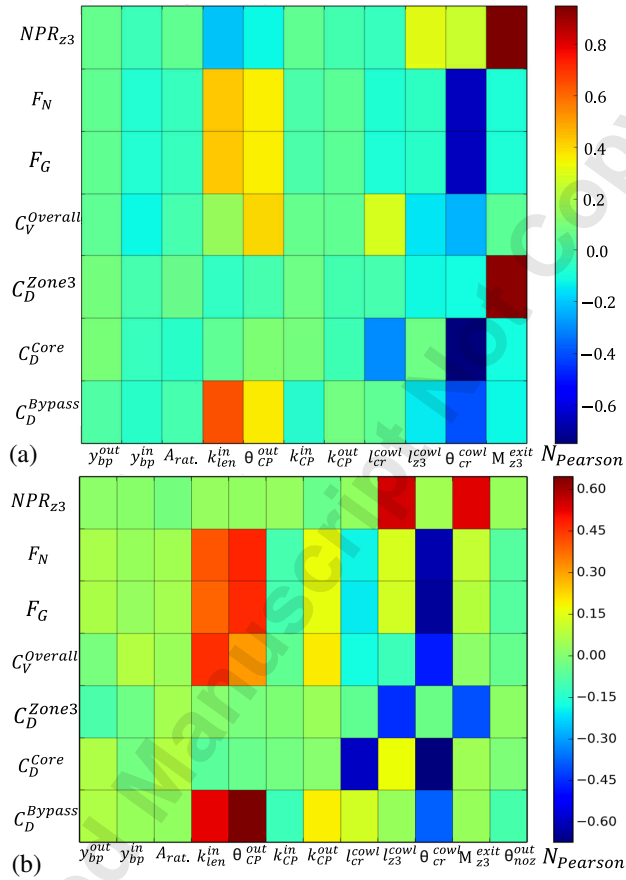
Fig. 17. Linear correlation estimation between design variables and performance metrics: (a) future $E1$ engine, (b) current $E2$ engine
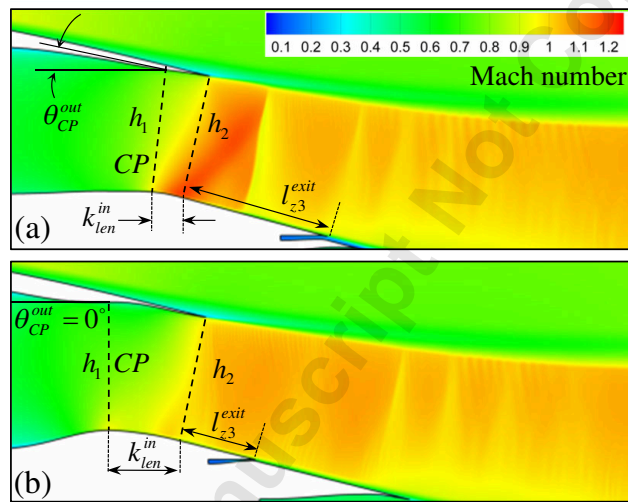
Fig. 18. Exhaust design improvement for the $E1$ future engine architecture: (a) Baseline exhaust nozzle, (b) Improved exhaust nozzle

2016-03-15

Aerodynamic design of separate-jet exhausts for future civil aero engines, Part I: parametric geometry definition and CFD approach

Goulos, Ioannis

ASME